Vibration-resistant phase-shifting interferometry

Leslie Deck

A method to reduce the sensitivity of phase-shifting interferometry to external vibrations is described. The returning interferogram is amplitude split to form two series of interferograms, taken simultaneously and with complementary properties, one with high temporal and low spatial resolution and the other with low temporal and high spatial resolution. The high-temporal-resolution data set is used to calculate the true phase increment between interferograms in the high-spatial-resolution data set, and a generalized phase-extraction algorithm then includes these phase increments when the topographical phases in the high-spatial-resolution data set are calculated. The measured topography thereby benefits from the best qualities of both data sets, providing increased vibration immunity without sacrificing high spatial resolution.

Key words: Interferometry, vibration, phase shifting.

1. Introduction

Phase-shifting interferometry[1] (PSI) is a technique often employed for noncontact precision surface metrology. PSI measures test surface topography by precisely measuring the phase angles in interferograms generated by light reflected from a reference surface and the test object. The process requires acquiring a sequence of interferograms while the reference phase is adjusted in a controlled manner. The interferogram intensities are described by

$$I'[x, y, \delta(t)] = I(x, y) + V(x, y)\cos[\phi(x, y) - \delta(t)], \quad (1)$$

where $\phi(x, y)$ is the unknown phase angle and $\delta(t)$ represents the time-dependent reference phase. The total intensity $I(x, y)$ and coherence modulus $V(x, y)$ are typically assumed to be constant throughout the acquisition. The reference-phase increment between interferograms is ideally a known constant and typically 90 deg. The interferometric phase at each point (or pixel) in the field of view is then determined by a filtering algorithm that uses the measured intensities from the interferogram sequence. Unfortunately, the presence of external vibrations corrupts the phase increment by an unknown amount, and these vibrationally induced distortions are often the dominant error source in phase-shifting applications. Much effort has been invested in understanding how vibration affects PSI metrology and in methods to reduce this sensitivity.[2–6] de Groot[7] has derived analytical formulas for the vibration sensitivity of the standard PSI algorithms in the small amplitude limit and shows that these algorithms will always be most sensitive to vibrations whose frequency equals half of the data rate. The most straightforward method of reducing vibrational effects is therefore simply to take interferogram data at higher rates, which would have the effect of pushing the sensitivity to higher frequencies at which natural sources of vibration are rarer, vibration amplitudes are reduced, and passive isolation systems are more efficient.

There are practical difficulties in this approach, however. Increasing the data bandwidth without sacrificing lateral resolution requires costly and rare state-of-the-art detectors. These high-speed, high-density arrays often have multiple, high bandwidth outputs, putting huge demands on the memory, bandwidth, and input architecture of the acquisition system. It is typical for these specialized arrays to cost tens of thousands of dollars and require a similarly costly acquisition system, making them difficult to incorporate into all but the most specialized interferometers. A number of investigators have tried to circumvent these difficulties with various strategies. For a single-point application, Smythe and Moore[2] used a homodyne receiver to produce an instantaneous quadrature phase measurement. In principle this completely eliminates vibrational effects, but it would be extremely difficult and costly to extrapolate their method to cover an area. Wizinowich[3] ex-

The author is with Zygo Corporation, 21 Laurel Brook Road, P. O. Box 448, Middlefield, Connecticut 06455-0448.

Received 28 September 1995; revised manuscript received 23 May 1996.

0003-6935/96/346655-08$10.00/0

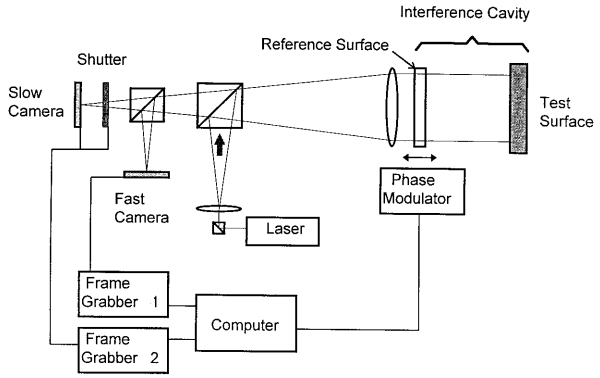

Fig. 1. Diagram of the apparatus necessary to implement the two-camera PSI method for large-aperture, Fizeau-type interferometers.

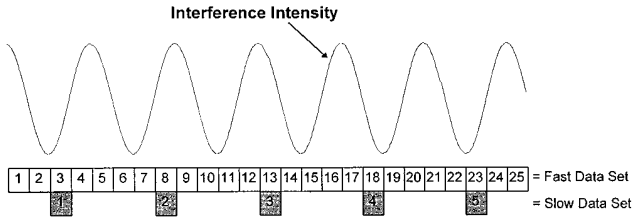

Fig. 2. Sampling sequence in which the slow data-set size is equal to five frames, and the fast:slow camera ratio is equal to five. The clear boxes correspond to the frames acquired by the fast camera; the shaded boxes correspond to the frames acquired by the slow camera. The box widths correspond to the frame integration time. Twenty-five fast camera frames are required for this sequence.

ploited the special capability of a particular area detector in a novel way to obtain full-field interferograms at high effective rates whereas Lai and Yatagai[6] required that the surface under test possess a tilted, flat region so that the high-frequency spatial fringes from this region can be used to estimate the true phase variation induced by the reference-phase shifter.

In this paper a method is described that couples two simultaneously acquired interferograms, taken with two common, commercially available, low-cost arrays with complementary capabilities, to provide vibration insensitivity equal to or exceeding that achievable with standard PSI techniques with a single high-performance imager. As with Lai and Yatagai, the method estimates the true phase variation induced by the reference-phase shifter but does not require the existence of any special surface features, making the method more generally applicable.

2. Method Description

The strategy is to use a commercially available low-speed, high-density sensor to image the full surface and provide the data set from which the surface profile is calculated and a high-speed, low-density sensor simultaneously imaging the same field to provide a way to measure the true phase increment between the low-speed interferograms. I refer to this technique as the two-camera PSI (2CPSI) to distinguish it from standard PSI methods. A diagram of the apparatus as configured for a large-aperture application is shown in Fig 1. The interferogram is amplitude split and simultaneously imaged onto the two sensors. The fast sensor acquires an interferogram, or frame, every phase increment δ, typically 90 deg. This sequence of acquired interferograms is called the fast data set (FDS) and corresponds to a traditional PSI data set whose form is given by Eq. (1):

$$I_I'(x, y, \delta) = I(x, y) + V(x, y)\cos[\phi(x, y) - \delta i]. \quad (2)$$

The index i runs over all the N_F frames in the FDS, $i = 0, \ldots, N_F - 1$. Note the assumption of the constant phase increment in the FDS. The slow sensor is synchronized with the fast sensor and is shuttered to have the identical frame integration period. The sequence of acquired interferograms from the slow detector is called the slow data set (SDS) and consists of frames acquired with an integer multiple of FDS frames between them (i.e., nominally separated in phase by an integer multiple of δ). There is considerable latitude in the choice of sampling sequence. However, for best results the sampling sequence must satisfy two rules: The minimum size of the SDS is three frames [because $I(x, y)$, $V(x, y)$, and $\phi(x, y)$ in Eq. (1) are constant but unknown], and the sampling sequence must maximize the sampling of independent parts of the interference cycle (i.e., parts whose phases are not equal modulo 2π). Failure to observe these rules can lead to increased error in the SDS phase determination or, in extreme cases, to complete phase indeterminacy. One constant interval sampling sequence that satisfies this criterion well is shown in Fig. 2 where the SDS size is five frames and the separation between the SDS frames is five FDS intervals (a 5:1 fast:slow camera frame rate ratio) for a nominal phase increment of 5δ or $5\pi/2$ between SDS frames. Each of the four parts of the interference cycle are sampled at least once. Other constant interval sampling functions that work well for an SDS size of five frames include separations of odd integers of $\pi/2$, such as $7\pi/2$, $9\pi/2$, $11\pi/2$.

The sequence of N_S SDS interferograms is given by

$$I_j''(x, y, \Delta_j) = I_{S(j)}'(x, y, \delta), \quad (3)$$

where $j = 0, \ldots, N_S$ and the sampling sequence $S(j)$ defines which FDS frame intervals are used in the SDS. For the example shown in Fig. 2,

$$S(j) = 2 + 5j,$$

where $j = 0, \ldots, N_S$ and $N_S = 5$. The SDS phase increments Δ_j are now determined by a PSI analysis of the FDS. The SDS phase increments for any particular field point either are calculated from the nearest-neighbor FDS point or are interpolated from the phase increments derived from the group of

nearest-neighbor FDS points. The phase at each frame i of the FDS is first calculated with a conventional PSI phase-extraction function,

$$\Phi_i(x, y) = \mathrm{PSI}[I(x, y, \delta), i], \tag{4}$$

where the PSI function uses the intensities measured about frame i in a manner dependent on the choice of the phase-extraction algorithm. For example, the well-known five-frame algorithm introduced by Schwider *et al.*[8] would use

$$\mathrm{PSI}[I(x, y, \delta), i] = \tan^{-1}\left\{\frac{2[I_{i-1}(x, y, \delta) - I_{i+1}(x, y, \delta)]}{2I_i(x, y, \delta) - I_{i-2}(x, y, \delta) - I_{i+2}(x, y, \delta)}\right\}$$

The phases $\Phi_i(x, y)$ are then unwrapped temporally to eliminate the 2π discontinuities stemming from the cyclic nature of the interference:

$$\Phi_i = \Phi_i + 2\pi\ \mathrm{round}\left[\frac{\Phi_i(x, y) - \Phi_{i-1}(x, y)}{2\pi}\right] \quad \text{for } i = 1, \ldots, N_F, \tag{5}$$

where the round function rounds the quantity in brackets to the nearest whole number. The SDS phase increments are then given by

$$\Delta_j = \Phi_{S(j)} - \Phi_{S(0)} \text{ for } j = 0, \ldots, N_S - 1. \tag{6}$$

Following Greivenkamp,[9] one calculates the interferometric phase for each pixel in the SDS in a least-squares sense by the solution of the matrix equation with the interferometric phase $\phi(x, y)$ given by

$$\begin{vmatrix} N_S & \sum \cos(\Delta_j) & \sum \sin(\Delta_j) \\ \sum \cos(\Delta_j) & \sum \cos^2(\Delta_j) & \sum \cos(\Delta_j)\sin(\Delta_j) \\ \sum \sin(\Delta_j) & \sum \cos(\Delta_j)\sin(\Delta_j) & \sum \sin^2(\Delta_j) \end{vmatrix} \begin{vmatrix} a_0(x, y) \\ a_1(x, y) \\ a_2(x, y) \end{vmatrix} = \begin{vmatrix} \sum I_j''(x, y) \\ \sum I_j''(x, y)\cos(\Delta_j) \\ \sum I_j''(x, y)\sin(\Delta_j) \end{vmatrix}, \tag{7}$$

$$\phi(x, y) = \tan^{-1}\left[\frac{a_2(x, y)}{a_1(x, y)}\right]. \tag{8}$$

In this way the assumption of equal *a priori* known phase intervals is required only when one is calculating the phase variation of the FDS, where it is most likely satisfied.

For this method to work well requires that the FDS be taken at a fast rate compared with the frequency of vibrations present and that the phase-extraction algorithm used to calculate the FDS phases be very robust to small deviations in the phase interval; otherwise the SDS phase increment cannot be calculated from the FDS phases without appreciable error. Two phase-extraction algorithms were tested with 2CPSI, the five-frame algorithm of Schwider *et al.* mentioned above, and a recently derived seven-frame algorithm by de Groot.[10] Figure 3 shows the phase error calculated by these algorithms as a function of the phase-shift interval. Although the seven-frame algorithm is generally superior, both algorithms reproduce the true FDS phase variation very well for the range of vibrations typically found in PSI applications. This author has found that under most conditions algorithm choice is less important to 2CPSI performance than the FDS frame rate. On the other hand, if the vibration frequency is low relative to the FDS acquisition rate, the error in the phases calculated from the FDS is, to a good approximation, equal to the error induced by a linear phase-shifter miscalibration.[11,12] In the low-frequency limit these errors simply add, so the sensitivity of 2CPSI to phase-shifter miscalibration is in general equivalent to the sensitivity of the chosen FDS phase-extraction algorithm. This was verified through simulations, and a plot of the peak-to-valley (P–V) error in the calculated phase from 2CPSI as a function of the phase-shift interval for the two algorithm choices above produces curves identical to those in Fig. 3.

The minimum number of interferograms in the FDS, N_F, is determined by

$$N_F = A + \sum_{j=1}^{N_S-1} \frac{\delta_j - \delta_{j-1}}{\delta} = A + \sum_{j=0}^{N_S-1} M_j,$$

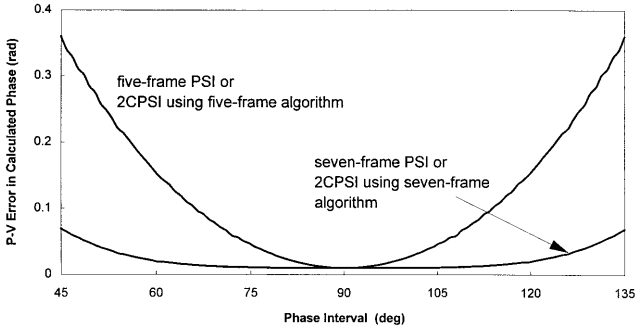

Fig. 3. Calculated P–V phase error for two different phase-extraction algorithms as a function of the phase interval. Identical curves are obtained with 2CPSI, depending on which algorithm is used for fast phase extraction. A phase offset of 0.01 rad has been added to both curves for clarity.

where A represents the number of frames required in the FDS phase-extraction algorithm and M_j is the number of FDS frames between SDS frames j and $j-1$. The additional A frames provide enough leader and trailer frames so that phases are calculable at the extremes of the SDS. For the example shown in Fig. 2 (five SDS interferograms with a 5:1 fast:slow frame rate ratio and five-frame algorithm) 25 interferograms are required for the FDS. If the phase shifting were accomplished by mechanically translating one of the legs of the interferometer, as is typically done, the total required translation for the example in Fig. 2 is less than 2 μm at He–Ne wavelengths, which is easily performed with commercial piezoelectric devices.

The matrix elements on the left-hand side of Eq. (7) should be evaluated for each of the N_F pixels in the FDS, so throughput considerations make it desirable to keep the sampling density of the high-speed sensor as low as possible. The sampling density depends on the application and the degree of field correction desired. For small-aperture applications we can correct the entire aperture by replacing the fast sensor with a single-point detector.

Fourier-transform theory teaches that modifying the sampling function will change the frequency sensitivity. Thus the choice of how many interferograms to use in the SDS and their relative separations is fundamental to the performance of the method. This feature provides a way to tailor the measurement to minimize the sensitivity to vibrational frequencies that happens to be dominant in the environment. Much of what follows explores the consequences of the choice of sampling function.

3. Simulations

An analytical formulation of the method's performance similar to that in Ref. 2 is complicated by the use of a numerical technique for the phase calculation. Performance was therefore predicted through computer simulation. In the simulations the method's results are compared with conventional PSI techniques to investigate performance dependencies on various parameters. Following the prescription of a previous publication,[13] I modeled the intensity variation with the following equation:

$$I_{mj} = \int_{t_j}^{t_j+P} I_0 \left\{ 1 + C \cos\left[\frac{4\nu t \pi}{\lambda} + \theta_m + F \sin(2\pi\omega t + \varphi) \right] \right\} \mathrm{d}t,$$

where subscripts m, j refer to pixel and frame-sequence numbers, respectively, the quantity $(4\nu t\pi)/\lambda$ represents the phase induced by the phase shifter alone, θ_m is the topographical phase at pixel m, I_0 is the dc intensity, C is the interference contrast, and F, ω, φ are the amplitude, frequency, and phase offset of the vibrational disturbance. The integral is performed over the pixel integration period P, determined by the camera frame rate and requirement that the FDS phase increment be nominally equal to δ (90 deg in this paper). A number of data sets with N linearly varying vibrational phase offsets spanning 2π in phase are then generated for a series of M pixels whose topographical phase also covers 2π. The rms deviation is calculated by

$$E_{\mathrm{rms}} = \left[\frac{1}{M} \frac{1}{N} \sum_{m=1}^{M} \sum_{n=1}^{N} ({\theta_m}^{2C} - {\theta_m}^{T})^2 \right]^{1/2},$$

where ${\theta_m}^{2C}$ is the topographical phases calculated with the 2CPSI method and ${\theta_m}^{T}$ is the true topographical phases for pixel m.

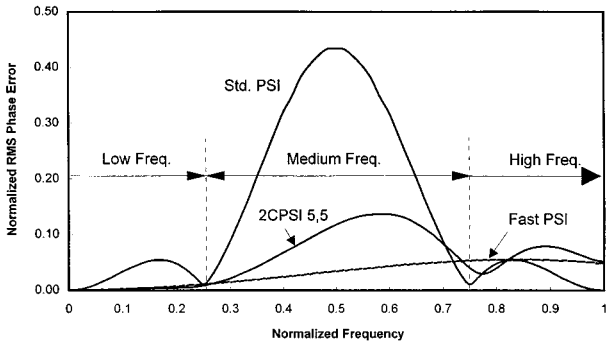

Fig. 4. Vibration-sensitivity spectra at small vibration amplitudes for PSI with data acquired at the slow camera rate (Std. PSI), PSI with data acquired at the fast camera rate (Fast PSI), and two-camera PSI for a slow camera data-set size of five frames and a 5:1 fast:slow camera rate ratio (2CPSI 5,5). The phase error is normalized to the vibration amplitude, and the frequency is normalized to the slow camera rate. Also indicated are the boundaries of the low-, medium-, and high-frequency regimes discussed in the text.

Figure 4 shows the simulation predictions for the vibration-sensitivity spectrum for 2CPSI with an SDS size of five frames and a nominally $5\pi/2$ phase interval between frames. Because the performance of 2CPSI depends so critically on the nature of the sampling function, all 2CPSI results shown indicate the sampling function used by following the 2CPSI identifier with the size of the SDS and the fast:slow frame rate ratio separated with a comma. For example, the 2CPSI 5,5 identifier in Fig. 4 represents results when a five-frame SDS and a 5:1 fast:slow frame rate ratio are used.

Furthermore, all vibration-sensitivity spectra are shown as a function of normalized variables. The rms error is normalized to the vibration amplitude, and the vibration frequency is normalized to the slow camera frame rate. In this way the results can be easily adapted to a variety of acquisition rates and vibrations. The predictions for standard PSI (where constant phase intervals are assumed) taken at the speeds of the slow camera rate (Std. PSI) and at a rate five times the slow camera rate (Fast PSI) are also shown in Fig. 4 for comparison. These predictions hold for vibration amplitudes whose interferometric phase excursions are small compared with 2π, which are vibration amplitudes typically found in PSI ap-

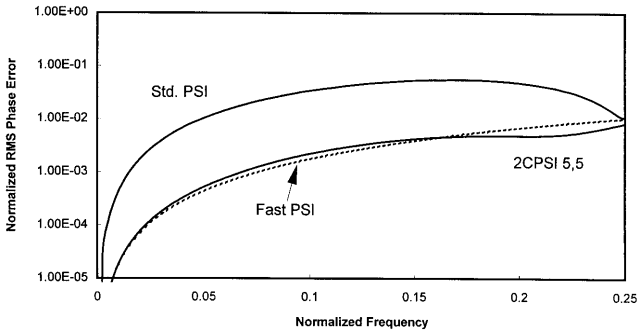

Fig. 5. Close-up of the vibration sensitivity for 2CPSI 5,5, standard PSI, and Fast PSI in the low-frequency regime.

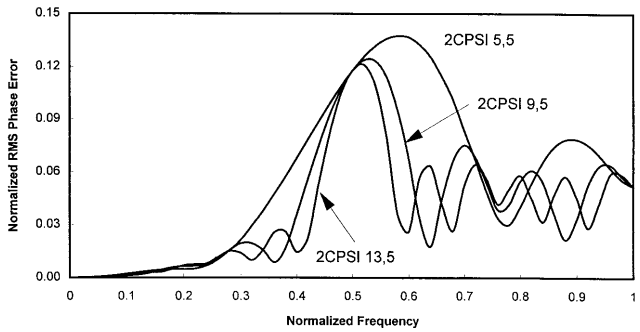

Fig. 7. Vibration-sensitivity spectra for different slow data-set sizes in 2CPSI.

plications. The figure is split into three frequency regimes: low (less than 0.25), medium (between 0.25 and 0.75), and high (greater than 0.75). The residual 2CPSI 5,5 sensitivity is due to the finite SDS integration period, and the peak sensitivity is a factor of 3 smaller than Std PSI. The low-frequency regime (normalized frequencies of less than 0.25) is particularly important because these frequencies are difficult to suppress with passive isolators. Figure 5 is a log plot of the vibration-sensitivity spectrum in the low-frequency regime. At these frequencies the reduction in vibration sensitivity offered by 2CPSI 5,5 is significantly greater than the Std. PSI and is effectively equivalent to Fast PSI. In most conditions, however, the overall sensitivity spectrum of 2CPSI is inferior to the spectrum obtained if it were possible to acquire the high-density interferograms at the fast camera rate—as one can see by comparing the Fast PSI and 2CPSI 5,5 curves.

Figure 6 confirms that for constant slow camera frame rates, the vibration sensitivity is reduced as the frame rate of the high-speed camera is increased. The curves represent vibration-sensitivity spectra for fast:slow camera frame rate ratios of 5, 7, 9, and 13 with an SDS size of five frames and the phase separation between slow camera frames adjusted to provide identical slow camera frame rates. For comparison, the vibration-sensitivity curve for Fast PSI is also included. Once the fast:slow camera frame rate ratio is greater than 7, the 2CPSI method achieves similar vibration immunity to Fast PSI over the frequency spectrum shown.

Increasing the number of slow frames has the effect of narrowing the 2CPSI sensitivity spectrum at medium frequencies but does not reduce the sensitivity at the peak. The rest of the sensitivity more closely follows the sensitivity of standard PSI that uses the FDS frame rate. This is illustrated in Fig. 7, which shows the sensitivity curves for 2CPSI with SDS sizes of 5, 9, and 13.

As mentioned above, the phase separation between the slow frames need not be nominally constant. One can tailor the acquisition to adjust the frequency sensitivity and minimize the errors to one's particular environment. Figure 8 shows the frequency sensitivity for a five-frame SDS acquisition whereby the separation between SDS frames was sequentially increased by one FDS frame. This chirped acquisition set offers reduced sensitivity in the mid-frequency range relative to both Std PSI and 2CPSE 5,5 at the cost of increased sensitivity at high frequencies. If the operating environment contained significant power in the midfrequency range, perhaps because of a resonance or background machinery operating at those frequencies, a chirped acquisition might provide greater vibration immunity.

4. Experimental Results

To test the method and verify the predictions of the simulations, the experimental apparatus shown in

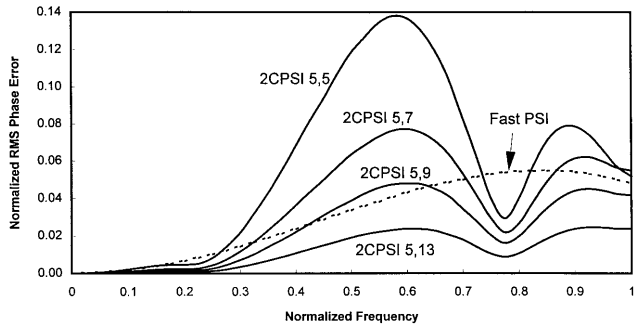

Fig. 6. Vibration-sensitivity spectra for different fast:slow camera speed ratios in 2CPSI for small amplitude vibrations. A PSI analysis of data acquired at a speed 5 times faster than standard (Fast PSI) is shown for comparison.

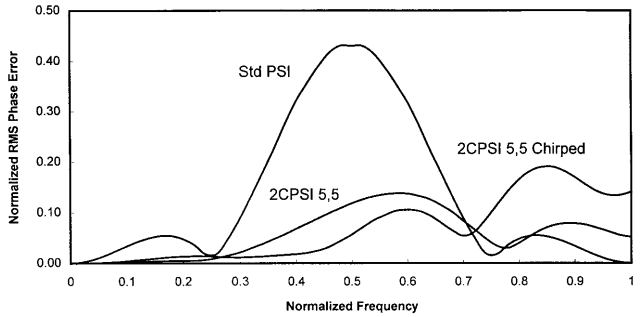

Fig. 8. Vibration-sensitivity spectra for chirped 2CPSI 5,5 compared with 2CPSI 5,5 and standard PSI for small-amplitude vibrations.

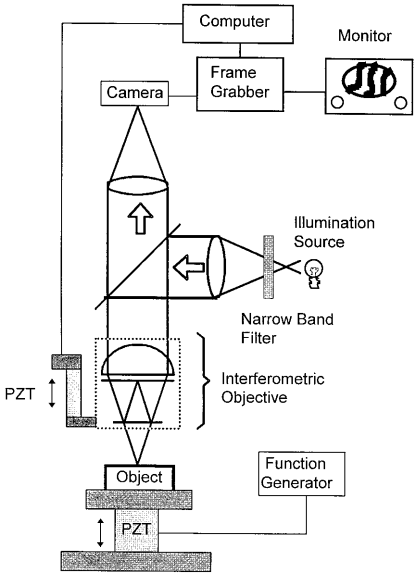

Fig. 9. Diagram of the experimental apparatus used to test the 2CPSI method.

Fig. 9 was constructed. An interferometric microscope imaged the surface under test onto a CCD camera operating at 25 Hz. The interferometric objective was translated along the optical axis at a constant velocity with a piezoelectric translator (PZT) to perform the phase modulation function. The sample rested on top of another PZT that was driven with a sinusoidal voltage waveform to produce vibrational disturbances at a particular frequency and amplitude. A frame grabber digitized the camera images to 8 bits at the camera frame rate and saved the digital images to a PC. From this sequence of images the FDS and SDS were constructed. The FDS consisted simply of a sequence of all consecutive intensity values from a single pixel whereas the SDS was constructed from a subset of all the acquired images and consisted of a sequence of frames each separated by a fixed number of frames. By varying the number and separation of the chosen frames, one can test different SDS sampling functions. Because the phase of the vibrational disturbances could not be controlled, an ensemble of data sets at a particular vibrational amplitude and frequency was analyzed and the rms deviation of the ensemble was calculated. For a particular vibrational amplitude the plot of rms deviation as a function of frequency is equivalent to the sensitivity spectrum, and these data could then be directly compared with the results from simulations.

Figure 10 compares the vibration-sensitivity spectra from simulations (curves) to the measured spectra (points) for the 2CPSI 5,5 method, PSI at the slow camera rate (Std. PSI), and PSI at the fast camera rate (Fast PSI). The sample measured was smooth and flat. The vibrational amplitude was fixed at 0.7 rad. The 2CPSI results were independent of the pixel chosen for the FDS, which agrees with the expectation that in a small-aperture application the

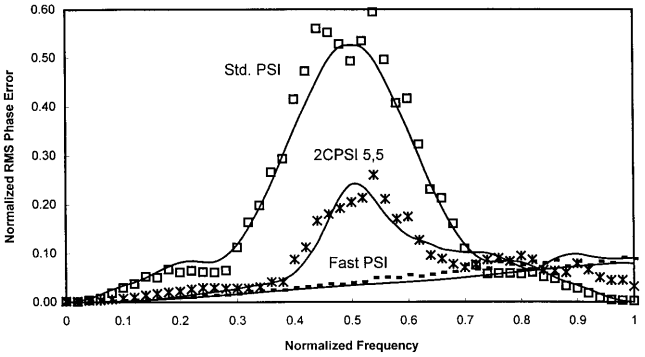

Fig. 10. Vibration-sensitivity spectra comparisons between simulation (curves) and experiment (points) for 2CPSI, Std. PSI, and Fast PSI.

vibrational disturbance is, to a good approximation, constant across the aperture. The reduction in vibration sensitivity shown in the 2CPSI results in good agreement with simulation. The small difference in the shape of the sensitivity spectra between Fig. 4 and 10 is due to the relatively large vibrational amplitude used in acquiring the data for Fig 10.

Figures 11 and 12 demonstrate the agreement in vibration sensitivity between simulation and experiment for different sampling functions. Figure 11 shows a comparison for an SDS size of 11 with a five-frame separation between SDS samples, and Fig. 12 shows the measured sensitivity for an SDS size of 5 with a sample spacing of nine frames. The gross features in both graphs are in good agreement with simulation; the mismatch in some of the detail could be due to the presence of insufficiently damped environmental vibrations in the experimental setup that were unaccounted for in the simulation.

As a practical demonstration of the reduction in vibration sensitivity afforded by this approach, Fig. 13 shows a measurement of an 86-nm step height standard in the presence of vibrations with a normalized frequency of 0.4 and an amplitude of 70 nm P–V. Three profiles are shown, a 2CPSI measurement with a 5:1 fast:slow frame rate ratio and an SDS size of five frames, a standard PSI measurement taken at the FDS rate (Fast PSI), and a standard PSI measure-

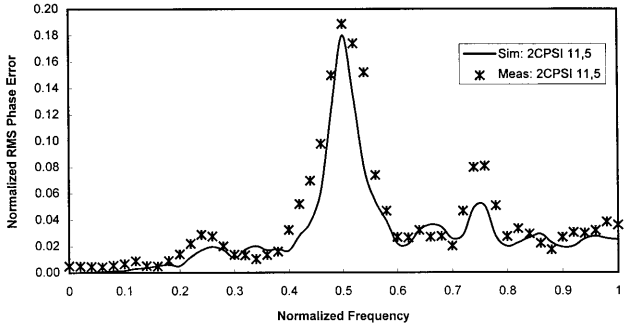

Fig. 11. Vibration-sensitivity spectrum comparison between simulation and experiment for 2CPSI with an SDS size of 11 frames and a 5:1 fast:slow frame rate ratio.

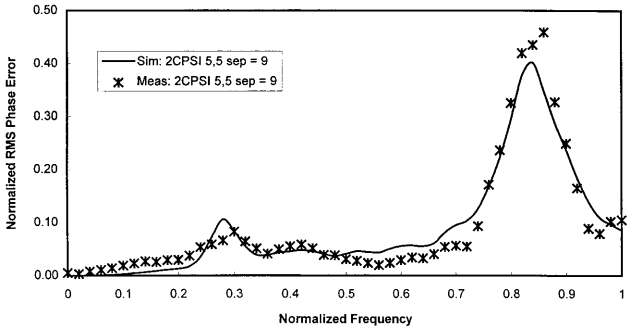

Fig. 12. Vibration-sensitivity spectrum comparison between simulation and experiment for 2CPSI with an SDS size of five frames and a 5:1 fast:slow frame rate ratio but with the SDS frame separation set to nine frames.

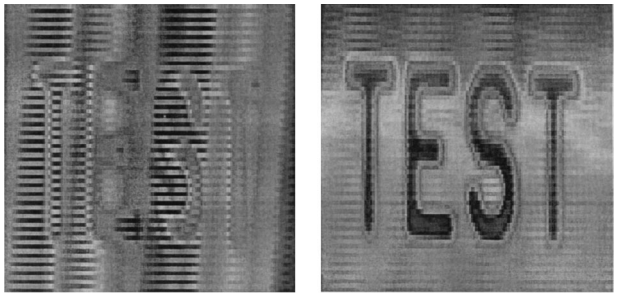

Fig. 14. Measurement of an 86-nm step-height standard in the presence of vibration with a 70-nm amplitude and normalized frequency of 0.4 when 2CPSI 5,5, Std. PSI, and Fast PSI are used. The performance of 2CPSI 5,5 was equivalent to Fast PSI. For clarity, +20 nm was added to the Fast PSI profile, and 20 nm was subtracted from the 2CPSI profile.

ment at the SDS rate (Std. PSI). For clarity the Fast PSI and 2CPSI measurement profiles are offset from zero by 20 nm in opposite directions. The Std. PSI profile was obviously distorted and produced a step height of 82 nm, a 4.6% error. The steps calculated from 2CPSI and Fast PSI were 86.8 and 86.2 nm, respectively, and in both profiles distortions were barely discernible.

Another striking, although admittedly qualitative, demonstration is shown in Fig. 14, which is a three-dimensional gray-scale profile of an embossed region of a step standard in the presence of vibrations with a normalized frequency of 0.4 and a P–V amplitude of 70 nm. The image on the left was obtained by a standard PSI analysis; the word TEST, etched into the surface to a depth of ~80 nm, is almost completely invisible among the vibrationally induced distortions. The even–odd row structure is a consequence of using an interlaced camera for data acquisition. The two interlaced fields are acquired at different times and thus have a phase offset between them. The time difference between the fields is well known, so the phase offset can, in the absence of vibrations, be simply subtracted out. Vibrations destroy this simple relationship, and the resulting profile, when analyzed with standard PSI, has both vibrationally induced ripple and interlace error. The image on the right was obtained with a 2CPSI 5,5 analysis, assuming a constant phase offset between fields. The text is clearly readable and few distortions remain.

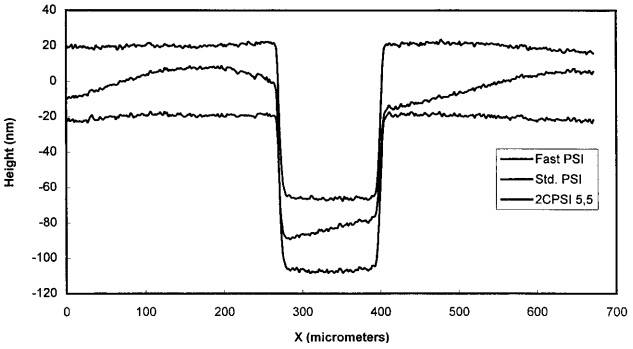

Fig. 13. Measurement of an 86-nm step-height standard in the presence of vibration with a 70-nm amplitude and a normalized frequency of 0.4 when 2CPSI 5,5, Std. PSI, and Fast PSI are used. The performance of 2CPSI 5,5 was equivalent to a fast PSI. For clarity, +20 nm was added to the Fast PSI profile, and 20 nm was subtracted from the 2CPSI 5,5 profile.

5. Discussion

To implement the 2CPSI method practically, the two cameras must have an identical frame integration period, strongly suggesting a frame transfer architecture, at least for the slow camera. The slow camera scene is integrated during one fast frame period and then read out during the intervening skipped frames. Eliminating scene smearing during readout may also require a shutter in front of the slow camera, although this feature is electronically available on some cameras. The decreased camera integration time requires a corresponding increase in illumination intensity to achieve the same level of photoinduced charge. This can become quite restrictive, especially for large fast:slow camera rate ratios. Large fast:slow camera rate ratios and/or large SDS sizes create another potential problem by quickly increasing the size of the FDS. A large FDS implies a large reference phase-shifter range, which, if the reference-phase shifting is done with piezoelectric transducers, can exceed the usable range of the transducer. Small-aperture interferometers can suffer from the additional effect of coherence loss when far from the zero optical path condition owing to illumination spectral bandwidth and/or objective defocus, invalidating the assumption of the constant $V(x, y)$ in Eq. (2).

Large-aperture interferometers will likely require field-dependent phase corrections. It is therefore important to sample the field with the fast sensor at a spatial density that is high compared with the shortest spatial vibrational period to be corrected. For many cases of interest, such as twisting of the reference flat during phase shifting or drumheadlike vibratory modes in either the reference or the test surface, only the first few low-order vibrational modes are excited with any appreciable amplitude, so

the sampling density need not be very great. Sensors with 16×16 or 32×32 pixel architectures are readily available and can operate with frame rates in the kilohertz range. The additional computational and storage burden imposed by the calculation of the phase variation of a thousand points is small considering today's computing capabilities. However, a single pixel must still cover a small area compared with the local fringe spatial period, and this points to sensors with a small fill factor; otherwise only surfaces with gentle curvatures can be profiled reliably.

A final point on how the SDS phase increments Δ_j [Eq. (6)] are calculated is pertinent. There may be times when the phase-correction variation across the field is large enough that simply using the nearest-neighbor FDS points to calculate Δ_j produces patching, small phase discontinuities between the nearest-neighbor boundaries centered about each FDS point. Patching can sometimes be caused by an error in the phase-correction measurements alone. One can eliminate it by interpolating the measured phase increments for each SDS point between neighboring FDS points. This means that the matrix, Eq. (7), must be formed for each SDS point, significantly increasing the processing required to generate the profile.

6. Summary

In this paper a technique has been introduced to achieve high effective interferogram acquisition rates at high spatial density by acquiring two simultaneous interferograms with complementary properties: a high-speed, low-density interferogram and a low-speed high-density interferogram. The interferograms can be taken with commercial low-cost sensors, and the data are analyzed so that the measurement benefits from the best qualities of both data sets, providing increased vibration immunity without sacrificing high spatial resolution. Experiments in which the technique is used were performed with a small-aperture interferometric profiler, and the measurements were found to be in good agreement with the predictions of computer simulations. By simple adjustments of the acquisition parameters, the method's vibration sensitivity could be modified to best mitigate the effects of environmental vibration. The technique finds exceptional utility when lateral resolution requirements force the use of relatively slow high-density imaging arrays.

The author thanks Peter de Groot for many helpful discussions.

References

1. J. E. Greivenkamp and J. H. Bruning, "Phase shifting interferometry," in *Optical Shop Testing*," D. Malacara, ed. (Wiley, New York, 1992), Chap. 14.
2. R. Smythe and R. Moore, "Instantaneous phase measuring interferometry," Opt. Eng. **23,** 361–364 (1984).
3. P. L. Wizinowich, "Phase shifting interferometry in the presence of vibration: a new algorithm and system," Appl. Opt. **29,** 3271–3279 (1990).
4. C. T. Farrell and M. A. Player, "Phase-step insensitive algorithms for phase-shifting interferometry," Meas. Sci. Tech. **5,** 648–652 (1994).
5. I. Kong and S. Kim, "General algorithm of phase-shifting interferometry by iterative least-squares fitting," Opt. Eng. **34,** 183–188 (1995).
6. G. Lai and T. Yatagai, "Generalized phase-shifting interferometry," J. Opt. Soc. Am. A **8,** 822–827 (1991).
7. P. de Groot, "Vibration in phase-shifting interferometry," J. Opt. Soc. Am. A **12,** 354–365 (1995).
8. J. Schwider, R. Burow, K.-E. Elssner, J. Gizanna, R. Spolaczyk, and K. Merkel, "Digital wave-front measuring interferometry: some systematic error sources," Appl. Opt. **22,** 3421–3432 (1983).
9. J. E. Greivenkamp, "Generalized data reduction for heterodyne interferometry," Opt. Eng. **23,** 350–352 (1984).
10. P. de Groot, "Derivation of algorithms for phase-shifting interferometry using the concept of a data-sampling window," Appl. Opt. **34,** 4723–4730 (1995).
11. K. Kinnstaetter, A. W. Lohmann, J. Schwider, and N. Streibl, "Accuracy of phase shifting interferometry," Appl. Opt. **27,** 5082–5089 (1988).
12. C. Joenathan, "Phase-measuring interferometry: new methods and error analysis," Appl. Opt. **33,** 4147–4155 (1994).
13. P. de Groot and L. Deck, "Numerical simulations of vibration in phase shifting interferometry," Appl. Opt. **35,** 2172–2178 (1996).